# Nanoscale

Accepted Manuscript


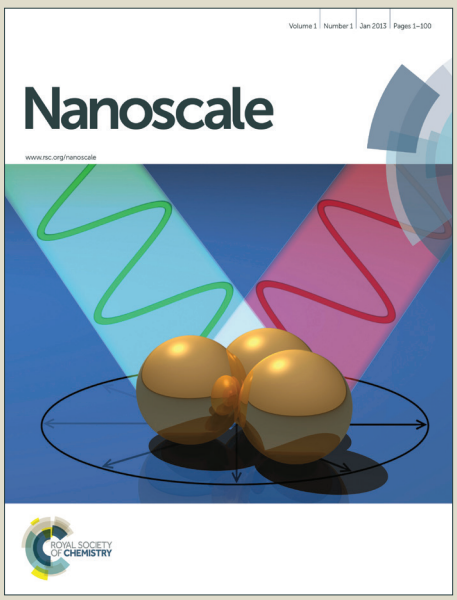





ROYAL SOCIETY OF CHEMISTRY

www.rsc.org/nanoscale

# Hierarchical Nanostructured $WO_3$–$SnO_2$ for Selective Sensing of Volatile Organic Compounds

Arpan Kumar Nayak,[1] Ruma Ghosh,[2] Sumita Santra,[3] Prasanta Kumar Guha,[2] Debabrata Pradhan,[1,*]

[1] *Materials Science Centre, Indian Institute of Technology, Kharagpur, W. B. 721 302, India*

[2] *Electronics and Electrical Communication Department, Indian Institute of Technology, Kharagpur, W. B. 721 302, India*

[3] *Department of Physics, Indian Institute of Technology, Kharagpur, W. B. 721 302, India*

E-mail: deb@matsc.iitkgp.ernet.in

*Support Information Available.*

**Abstract**

It remains a challenge to find a suitable gas sensing material that shows high response and selectivity towards various gases simultaneously. Here we report a mixed metal oxide $WO_3$–$SnO_2$ nanostructured material synthesized *in situ* by a simple, single-step, and one-pot hydrothermal method at 200°C in 12h, and demonstrate its superior sensing behavior towards volatile organic compounds (VOCs) such as ammonia, ethanol, and acetone. The $SnO_2$ nanoparticles with controlled size and density are uniformly grown on the $WO_3$ nanoplates by varying the tin precursor. The density of $SnO_2$ nanoparticles on $WO_3$ nanoplates plays a crucial role to the VOC selectivity. The response of present mixed metal oxides is found to be much higher than the reported results based on the single/mixed oxides and noble metal-doped oxides. In addition, the VOC selectivity is found to be highly temperature-dependent with optimum performance obtained at 200°C, 300°C, and 350°C for ammonia, ethanol, and acetone, respectively. The present results on the cost-effective noble metal-free $WO_3$–$SnO_2$ sensors can find potential application in human breath analysis by noninvasive detection.

**Keywords:** Gas sensing, mixed oxides, $WO_3$ nanoplates, ammonia, ethanol, acetone, heterojunction

## Introduction

Development of low-cost, ultrasensitive, and highly selective chemical sensors which can sense trace amount of volatile organic compounds (VOCs) have become indispensable for environmental monitoring, biomedical, and industrial applications.[1] One of the vital biomedical applications of such ultrasensitive sensors can be as-breathe analyzer, in which array of sensors need to detect very low concentration of VOCs such as acetone (in case of diabetics), nitric oxide (in case of asthma), and ammonia (in case of renal diseases) from exhaled human breathe.[2] The current breathe analysers are based on gas chromatography and mass spectrometry, which are large, expensive, and require pre-concentration procedures for reliable measurement.[3,4,5] One of the suitable alternatives is portable metal oxide based chemo-resistors with high sensitivity and selectivity towards a particular biomarker.[6]

Metal oxide based chemo-resistive sensors has shown significant potential because of their high sensitivity towards different analytes with fast response and recovery.[7] However, selectivity has always been an issue for metal-oxide based sensors. In recent years, several metal oxides (such as $SnO_2$, $In_2O_3$, $TiO_2$, ZnO, and CuO) have been widely explored for different gas detections.[8,9,10,11,12] Among these, $SnO_2$ is one of the very promising and widely studied sensing materials. $WO_3$ is another important gas sensing material and various forms of $WO_3$ such as thin films, nanocrystals, hollow spheres, nanofibers, and nanorods have been extensively used for the detection of several gases and VOCs.[13,14,15,16,17,18,19] In majority of these studies, precious noble metals (Ag, Au, Pd, and Pt) are either doped or decorated into/on the metal oxides to improve the sensing performance (sensitivity and selectivity).[20,21,22,23,24,25,26,27] However, the use of noble metals increases the cost of the device and thereby prompting the researchers to explore non-noble metal-based sensors with competent performance for large-scale applications. There are a

few studies on metal doped and mixed metal oxides with much improved gas sensing properties.[28,29,30] In particular, Kim *et al.* reported an exceptionally fast CO response and recovery using NiO-doped hierarchical $SnO_2$ sensors.[31] Xu *et al.* have fabricated $In_2O_3$-$CeO_2$ nanotubes which acted as bifunctional gas sensors to detect $H_2S$ at low temperature (25–110°C) and acetone at relatively high temperature (300°C).[32] Recently, Kida *et al.* used the $SnO_2$ nanoparticles to control the porosity of $WO_3$ nanolamella to enhance the $NO_2$ sensitivity.[33]

Considering the effectiveness of $SnO_2$ and $WO_3$ nanostructures for sensing different gases, we report here *in situ* hydrothermal synthesis of $WO_3$–$SnO_2$ mixed metal oxide for the first time which can sense different VOCs selectively. The as-synthesized mixed metal oxides are composed of $WO_3$ nanoplates decorated with $SnO_2$ nanoparticles. The $SnO_2$ nanoparticles of three different concentrations were grown on the $WO_3$ nanoplates using a single-step hydrothermal technique by varying the tin precursor. Three important VOCs such as ammonia, ethanol, and acetone were tested on $WO_3$–$SnO_2$ based sensor and their performance has been compared with pure $WO_3$ nanoplates and $SnO_2$ nanoparticles. Not only was an improved sensing performance obtained with $WO_3$–$SnO_2$ but also with highly temperature-dependent selectivity towards different analytes. The high sensing response is ascribed to the multiple depletion regions formed between $WO_3$ and $WO_3$, $SnO_2$ and $SnO_2$, and $WO_3$ and $SnO_2$. Furthermore, the limit of detection (LOD) calculation shows that the present $WO_3$–$SnO_2$ based sensors can sense VOCs at ppb level (LOD for ammonia 520 ppb, LOD for ethanol 131 ppb, and LOD for acetone is 2.68 ppm) and thus they are appropriate for applications where trace amount of analytes need to detected (*e.g.* as breath analyzers). The importance of this work lies in (i) simple and cost effective *in situ* synthesis of $WO_3$–$SnO_2$ mixed metal oxide nanomaterials, (ii) sensors with large response towards three VOCs which are commonly used as biomarkers, and (iii) as-fabricated

sensors with high selectivity. This suggests that the development of such sensors will be highly beneficial for new generation highly sensitive and selective chemo-resistive sensors.

## Experimental Section

**Chemicals.** Sodium tungstate hydrate ($Na_2WO_4 \cdot 2H_2O$) and stannous choloride hydrate ($SnCl_2 \cdot 2H_2O$) from SRL, India; hydrochloric acid (HCl) about 35% v/v and oxalic acid ($C_2H_2O_4 \cdot 2H_2O$) from Merck, India, and Ethanol ($C_2H_5OH$) from Changshu Yangyuan Chemical, China. All the above reagents were analytical grade and used without further purification.

**Synthesis of $WO_3$ nanoplates.** $WO_3$ flowers-like structures self-assembled of nanoplates were prepared by using a facile hydrothermal method. In a typical synthesis, 1.6g sodium tungstate hydrate (0.12 M) was dissolved in 40 mL distilled water. Then 4 mL of concentrated HCl was added drop wise to the above transparent solution while stirring. The resulting solution turned yellow. Upon adding 1g oxalic acid (0.2 M) to above solution, it became transparent again. The final transparent solution was transferred to a 50 mL Teflon-lined stainless steel autoclave and sealed. The autoclave was heated at 200°C in a muffle furnace for 12h and then cooled to room temperature naturally. The precipitated product was collected by centrifuge and washed with ethanol and distilled water. The washed product was dried at 60°C for 4h and then calcined at 400°C for 2h under air.

**Synthesis of $SnO_2$ nanoparticles.** 0.54g stannous chloride hydrate (0.06 M) was dissolved in 40 mL distilled water and the solution was stirred for 5 min. Then 1 mL of concentrated HCl was added and stirred vigorously for 30 min prior to transferring it to a 50 mL Teflon-lined stainless steel autoclave. The autoclave was heated at 200°C for 12h and cooled naturally to room temperature. The as-synthesized product was washed and calcined as described for $WO_3$.

***In situ* Synthesis of $WO_3$–$SnO_2$ mixed oxides.** In the $WO_3$ synthesis as described above, upon adding oxalic acid to mixture sodium tungstate hydrate (0.12 M) and concentrated HCl, the solution becomes transparent. Then different quantity of stannous chloride hydrate (0.27g, 0.54g, and 1.08g) was added and stirred vigorously for 10 min before transferring it to autoclave. The autoclave was heated at same temperature for same duration (*i.e.* 200°C, 12h) and then cooled naturally to room temperature. The precipitated product was collected by centrifuge, washed, dried, and calcined as described for $WO_3$.

**Characterization.** The surface morphology of as-synthesized products was investigated using a Carl Zeiss SUPRA 40 field-emission scanning electron microscope (FESEM). The structural property of the products was measured with a PANalytical High Resolution XRD (PW 3040/60) operated at 40 kV and 30 mA with Cu Kα X-rays (1.54 Å) in the 2θ angle 20–80°. A FEI TECNAI G2 transmission electron microscope (TEM) was employed to investigate the detail microstructures of the samples. The energy dispersive X-ray (EDX) analysis of the samples was carried out using an EVO 60 Carl Zeiss SEM attached with Oxford EDS detector. The X-ray photoelectron spectroscopy (XPS) measurement was carried out using a PHI 5000 VersaProbe II Scanning XPS Microprobe with a monochromatic Al Kα source (1486.6 eV) with a typical energy resolution of 0.4−0.5 eV full width at half-maximum. The effective Brunauer–Emmett–Teller (BET) surface area of the as-synthesized samples was measured using a Quantachrome ChemBET analyzer.

**Gas sensing test.** The sensors were fabricated by dispersing $WO_3$, $SnO_2$, and $WO_3$–$SnO_2$ mixed metal oxide powder in ethanol and then drop casting on Pt-based interdigitated electrodes (IDEs) (Synkera Technologies) with 100 µm inter-fingers gap. The gas test measurements were carried out in a custom made gas test set-up. The set-up contains air tight stainless steel chamber

assembled with a heater, thermocouple, and probes. Mass flow controllers were used to vary the flow rates of gas analytes. Agilent 34972A LXI data acquisition card was used as an interfacing unit between the gas test set-up and computer, to record the resistance values of sensor samples at every 5 sec interval. The sensors were initially purged with dry air for 20 min to stabilize the baseline resistance at a particular temperature. Then they were exposed to target gases for 5 min followed by 10 min of dry air purging.

## Results and Discussion

### Morphology

The morphology of as-synthesized samples was studied by FESEM as shown in Figure 1. Figure 1(a) shows a representative FESEM image of $WO_3$ nanoplates, which are found to be self-assembled to near-spherical structure. Inset of Figure 1(a) shows a magnified FESEM image of nanoplates with 40–400 nm length/width and 20–60 nm thickness. Figure 1(b) shows FESEM image of uniform $SnO_2$ nanoparticles of diameter <20 nm. Figure 1(c), 1(d), and 1(e, f) show FESEM images of $WO_3$–($x$)$SnO_2$ mixed oxides synthesized by varying the tin precursor ($x$) *i.e.* 0.27g, 0.54g, and 1.08g $SnCl_2{\cdot}2H_2O$, respectively, while keeping tungsten precursor [$Na_2WO_4{\cdot}2H_2O$ (1.6g, 0.12 M)] constant. The plate-like morphology of $WO_3$ building blocks and their self-assembly to spherical flower-like morphology remains same by addition of tin precursor. Moreover, the density and size of $SnO_2$ nanoparticles were found to increase on the $WO_3$ nanoplates with increasing initial $SnCl_2.2H_2O$ concentration. At a lower tin precursor concentration *i.e.* $WO_3$–(0.27g)$SnO_2$, as shown in Figure 1(c), very fine particles of size 5–10 nm were observed on the nanoplates. These nanoparticles appear slighter brighter on the nanoplates as shown in the inset FESEM image of Figure 1(c). With increasing the tin precursor to 0.54g and 1.08g, the size of $SnO_2$ nanoparticles was found to be increased to ~20 nm and

20–40 nm, as shown in Figure 1(d) and 1(e, f), respectively. Insets of Figure 1(d, e, f) show magnified FESEM image clearly depicting bright $SnO_2$ nanoparticles deposited on the $WO_3$ nanoplates. At a higher tin concentration *i.e.* 1.08g $SnCl_2.2H_2O$, agglomeration of $SnO_2$ nanoparticles was found at a few locations as shown in Figure 1(f).

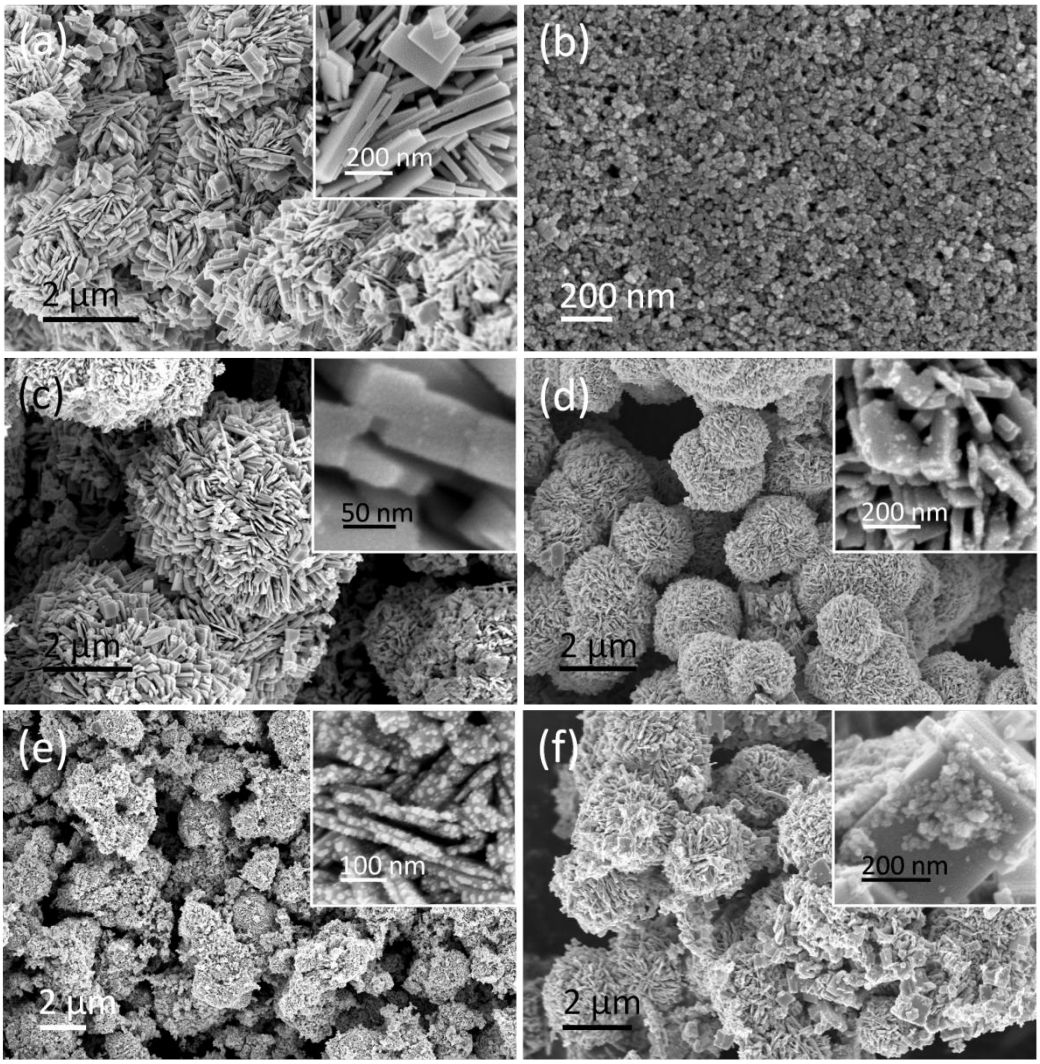


**Figure 1.** FESEM images of (a) $WO_3$ nanoplates, (b) $SnO_2$ nanoparticles, and (c) $WO_3$–(0.27)$SnO_2$, (d) $WO_3$–(0.54)$SnO_2$, and (e, f) $WO_3$–(1.08)$SnO_2$ mixed oxides prepared by varying $SnCl_2 \cdot 2H_2O$ concentration. Insets show magnified FESEM images of corresponding samples. All the samples were prepared hydrothermally at 200°C in 12h.

**Structural and microstructural analysis**

Figure 2 shows the XRD pattern of $WO_3$ nanoplates, $SnO_2$ nanoparticles, and $WO_3$–$SnO_2$ mixed oxides. The sharp diffraction features suggest the crystalline nature of all the samples. The XRD peaks of $WO_3$ nanoplates [Figure 2(a)] are readily indexed to the monoclinic crystal structure with the lattice parameters of a = 7.3, b = 7.53, and c = 3.83 (a = 7.384, b = 7.512, and c = 3.846, JCPDS No. 00-005-0363). The XRD pattern [Figure 2(b)] of $SnO_2$ nanoparticles matches the tetragonal cassiterite structure of $SnO_2$ with lattice constant a = 4.74 and c = 3.18 (a = 4.738 and c = 3.188, JCPDS No. 00-021-1250). The XRD patterns of all the $WO_3$–$SnO_2$ mixed oxides samples matched the monoclinic crystal structure of $WO_3$ without any other phases such as Sn or $SnO_2$ suggesting no change in the $WO_3$ crystal structure.[33] The absence of $SnO_2$ diffraction features in the mixed oxide sample is believed to be due to their small quantity. Nonetheless, the XRD intensity of $WO_3$ was found to increase with $SnO_2$ in the sample *i.e.* for $WO_3$–(0.27)$SnO_2$, $WO_3$–(0.54)$SnO_2$, and $WO_3$–(1.08)$SnO_2$ mixed oxides, as shown in Figure 2(c), 2(d), and 2(e), respectively. This increase in diffraction intensity indicates increase in the crystallinity, which can be attributed to incorporation of small amount of Sn into $WO_3$ lattice as reported earlier.[30]

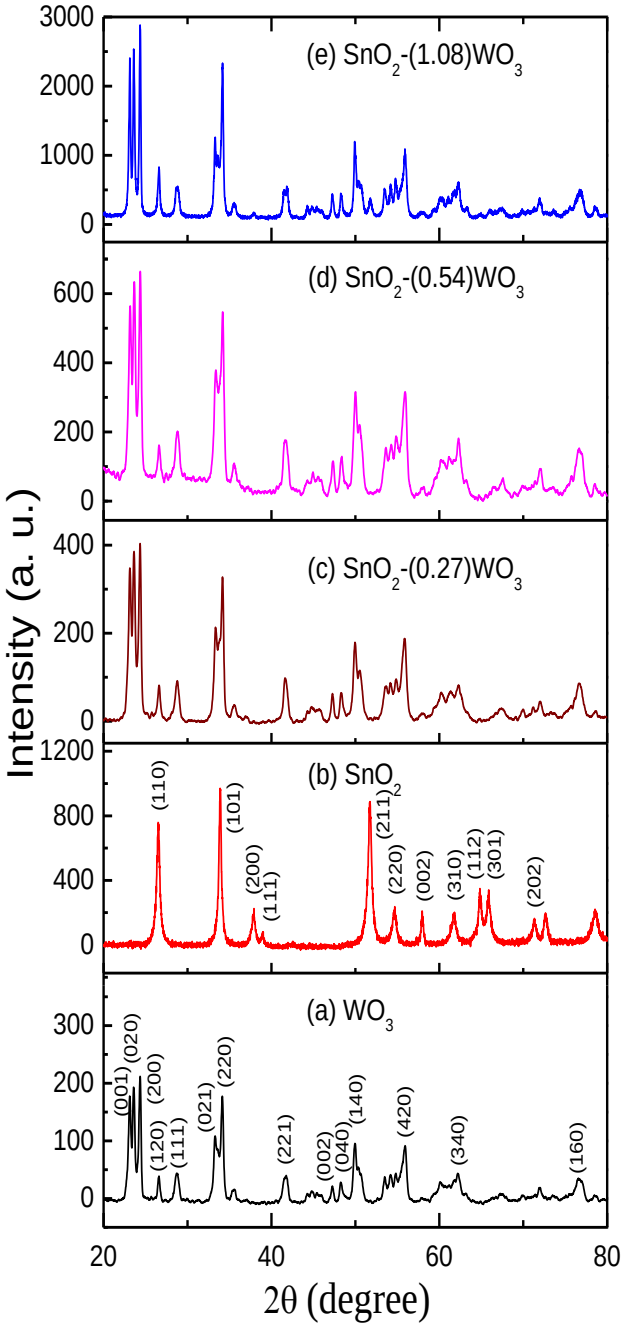


**Figure 2.** Powder XRD patterns of (a) $WO_3$ nanoplates, (b) $SnO_2$ nanoparticles, and (c) $WO_3$–(0.27)$SnO_2$, (d) $WO_3$–(0.54)$SnO_2$, and (e) $WO_3$–(1.08)$SnO_2$ mixed oxides prepared by varying $SnCl_2.2H_2O$ concentration in the hydrothermal process at 200°C in 12h.

The microstructures of the as-synthesized $WO_3$ nanoplates, $SnO_2$ nanoparticles, and $WO_3$–$SnO_2$ mixed oxides were examined by TEM. Figure 3(a) shows the TEM image of $WO_3$ nanoplates of either square or rectangle shape with size in the range of 40–400 nm. The high

resolution TEM (HRTEM) image [Figure 3(b)] taken at an edge of a nanoplate shows continuous lattice with a spacing of 3.77 Å, which corresponds to (020) plane.[33] The regular spot selected area diffraction pattern (SAED) as shown in the inset of Figure 3(b) confirms the single crystalline nature of $WO_3$ nanoplates. Figure 3(c) shows a TEM image of $SnO_2$ nanoparticles of size around 20 nm. An HRTEM image [Figure 3(d)] of $SnO_2$ nanoparticles shows the lattice fringe with a spacing of 2.65 Å indicating the crystalline nature of the particles. The distinct diffraction spots on the ring SAED pattern [inset, Figure 3(d)] further suggests the single crystalline nature of individual $SnO_2$ nanoparticles in accord to the XRD analysis.

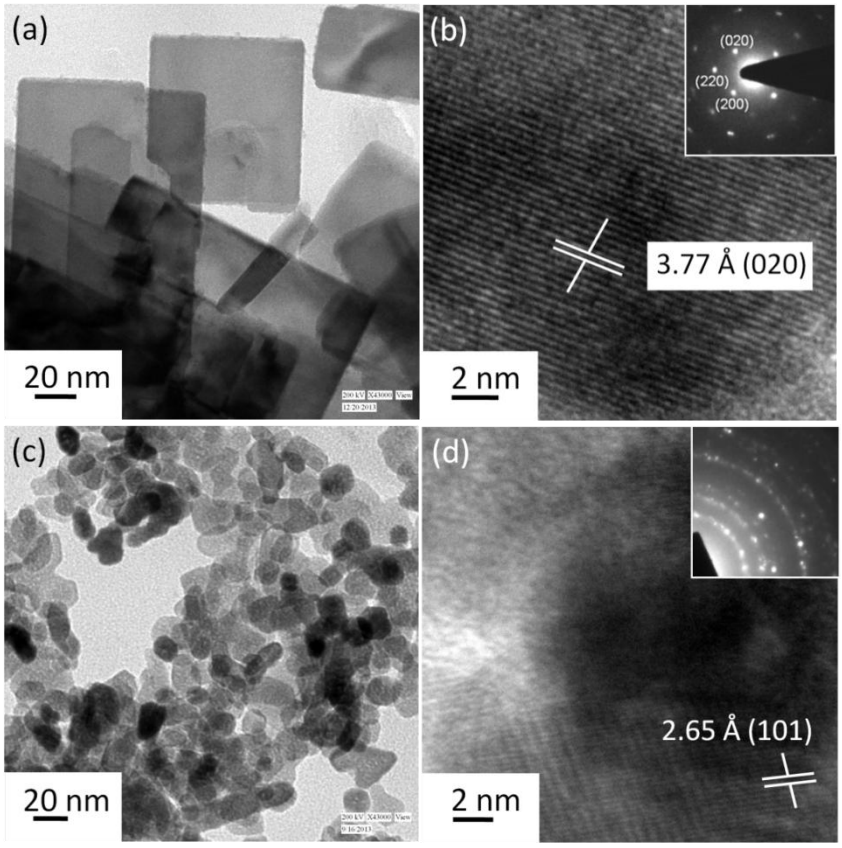


**Figure 3.** (a,c) TEM and (b,d) HRTEM images of (a,b) $WO_3$ nanoplates, and (c,d) $SnO_2$ nanoparticles. The insets of (b) and (d) display the corresponding SAED patterns.

Figure 4 shows the TEM image of $WO_3$–($x$)$SnO_2$ mixed oxides. The dark spots of size <10 nm on the $WO_3$ nanoplates in Figure 4(a) are believed to be $SnO_2$ nanoparticles of $WO_3$–(0.27)$SnO_2$. With increasing $SnCl_2 \cdot 2H_2O$ precursor to 0.54g and 1.08g in the synthesis, the size of $SnO_2$ nanoparticles was found to be increased to ~20 nm [Figure 4(b)] and 20–40 nm [Figure 4(c)], respectively, as clearly revealed in the TEM images. The number density of $SnO_2$ nanoparticles is found to be further increased with $SnCl_2 \cdot 2H_2O$ concentration. The HRTEM and spot SAED indicates no change in the crystal structure of $WO_3$ upon addition of tin precursor in the synthesis. Figure 4(d) shows a HRTEM image of $WO_3$ nanoplates of $WO_3$–(1.08)$SnO_2$ mixed oxide with a lattice spacing of 3.78 Å for the (020) planes of pure $WO_3$. It is important to note that no separate $SnO_2$ nanoparticles are found on the TEM grids for the $WO_3$–$SnO_2$ samples. This suggests that $SnO_2$ nanoparticles are grown and chemically bonded to $WO_3$ nanoplates. Furthermore, sensing experiments proved presence of heterojunction in the mixed oxide samples resulting enhanced response (discussed later), which could only be possible for chemically bonded materials.

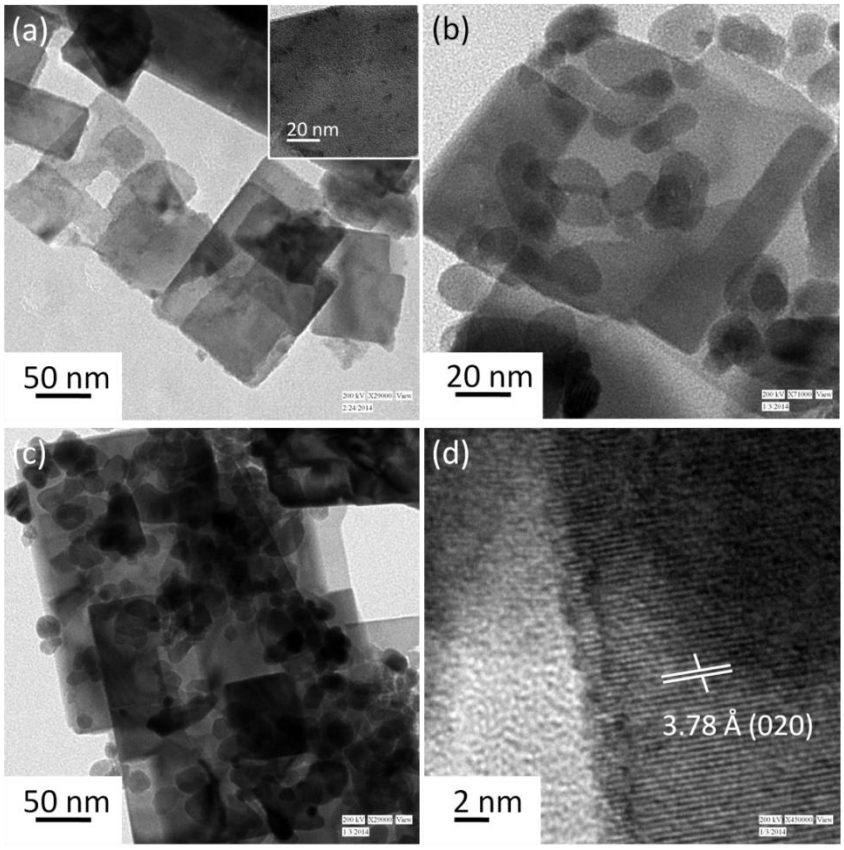


**Figure 4.** TEM images of (a) $WO_3$–(0.27)$SnO_2$, (b) $WO_3$–(0.54)$SnO_2$, and (c,d) $WO_3$–(1.08)$SnO_2$ mixed oxides prepared by varying $SnCl_2 \cdot 2H_2O$ concentration. Inset of (a) shows corresponding magnified image. (d) HRTEM image of an edge of $WO_3$ nanoplate shown in (c).

## Composition and chemical States

The elemental composition of as-synthesized samples was measured using energy dispersive X-ray (EDX) spectroscopy. Figure 5 shows the EDX spectra of pure $WO_3$ nanoplates, $SnO_2$ nanoparticles, and $WO_3$–(0.54)$SnO_2$ mixed oxides. The stoichiometry ratio of W and O match closely to $WO_3$ with slight oxygen deficiency. However, rest of the samples show higher oxygen composition than that of their stoichiometric ratio indicating surface oxygen and amorphous

hydroxides. The EDX spectrum [Figure 5(b)] from $SnO_2$ nanoparticles shows almost 6 at% higher oxygen, which can be ascribed to surface hydroxide [$Sn(OH)_4$] since tin is often found in +4 state. Moreover, Sn% was found to increase with increasing initial $SnCl_2 \cdot 2H_2O$ concentration used for the synthesis of $WO_3$–$SnO_2$ mixed oxides. This supports the morphology and microscopic results [Figure 1 and Figure 4] on increasing size and density of $SnO_2$ nanoparticles on the $WO_3$ nanoplates with increasing tin precursor concentration for the synthesis of mixed oxide.

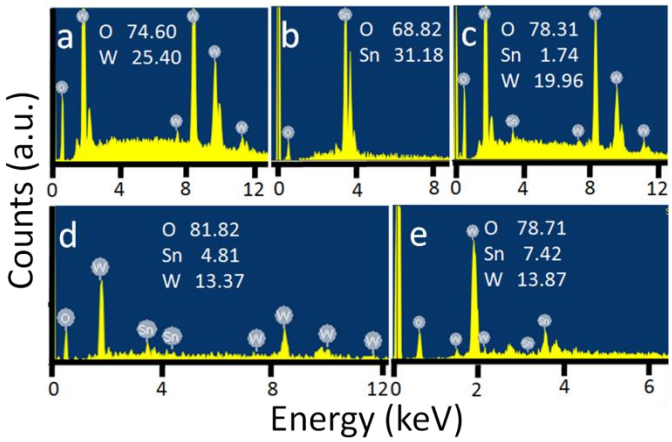


**Figure 5**. EDX spectra of (a) $WO_3$ nanoplates, (b) $SnO_2$ nanoparticles, and (c) $WO_3$–(0.27)$SnO_2$, (d) $WO_3$–(0.54)$SnO_2$, and (e, f) $WO_3$–(1.08)$SnO_2$ mixed oxides prepared with varying $SnCl_2 \cdot 2H_2O$ concentration.

The elemental and surface chemical states information was further obtained using X-ray photoelectron spectroscopy (XPS). Figure 6 shows the representative XPS spectra of $WO_3$–(1.08)$SnO_2$ mixed oxide. The survey spectrum [Figure 6(a)] confirms presence of W, Sn, and O along with surface impurity carbon. No peaks related to either Na or Cl (present in the precursors) in the survey spectrum suggests the high purity of the sample. The atomic percentages of W, Sn, and O were estimated to be 16.7%, 11.1%, and 72.2%, respectively. The

stoichiometry of $WO_3$ and $SnO_2$ is well matched from the atomic percentages. The Figure 6(b), 6(c), and 6(d) display the W 4f, Sn 3d, and O 1s region XPS spectra, respectively. The XPS peaks at 35.62 and 37.75 eV can be assigned to W $4f_{7/2}$ and W $4f_{5/2}$ of $WO_3$, respectively, with a spit-orbit spitting of 2.13 eV.[34,35,36] Similarly, the photoelectron peaks at 487.0 and 495.4 eV are assigned to Sn $3d_{5/2}$ and Sn $3d_{3/2}$, respectively.[37,38] The Sn XPS peaks confirm the +4 oxidation states contributed from $SnO_2$. The O 1s shows an intense peak at 530.5 eV of oxides and the broad O 1s peak at 531.8 eV can be assigned to surface hydroxides.[36]

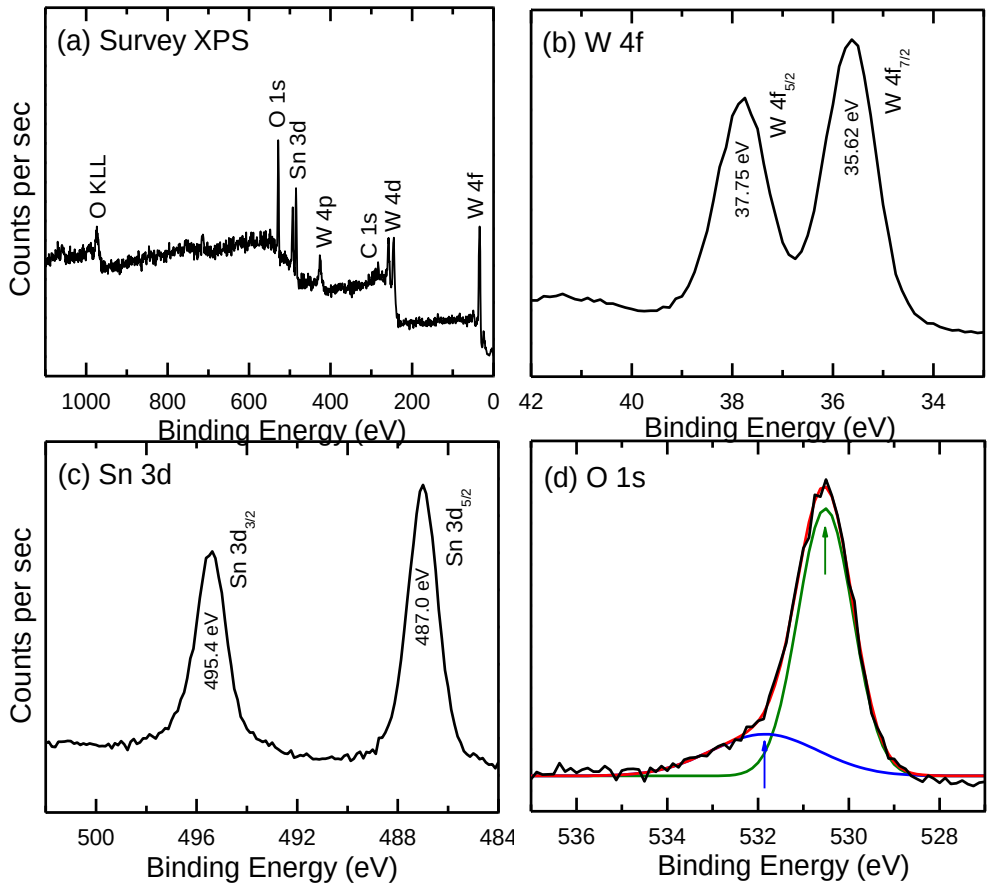


**Figure 6.** (a) Survey spectrum, and (b) W 4f, (c) Sn 3d, and (d) O 1s region XPS spectra of $WO_3$–(1.08)$SnO_2$ mixed oxide.

## Gas Sensing

The as-synthesized nanostructured mixed oxide material was drop-casted on platinum interdigitated electrodes to prepare the sensor device. In chemoresistive sensors, the resistance of the sensing layer changes in presence of the detectable gas. For testing the sensor devices, ammonia, ethanol, and acetone were selected because they are important vital biomarkers. The response of the chemoresistive sensors were calculated using equation (1).

$$\text{Response} = \frac{R_{air}}{R_{\text{VOCs}}} \quad (1)$$

where $R_{VOCs}$ is the resistance of the sensor material in presence of VOCs (ammonia/ethanol/ acetone) and $R_{air}$ is the resistance of the sensor material in presence of air. To explore the optimum performance of different sensor materials, temperature profiles of each of them were carried out for all the VOCs. Figure 7(a), 7(b), and 7(c) show the sensitivity response as a function of operating temperature for ammonia (1200 ppm), ethanol (350 ppm), and acetone (1000 ppm). The optimum response was obtained at 200°C for ammonia, 300°C for ethanol, and 350°C for acetone. These optimum temperatures are valid of all the sensing materials studied in the present work except for acetone. In case of acetone, $WO_3$–(0.54)$SnO_2$ and $WO_3$–(1.08)$SnO_2$ samples demonstrated optimum response at 300 ºC. The $WO_3$–$SnO_2$ mixed oxides were found to show higher response towards ammonia and ethanol compared to pure oxides ($WO_3$ and $SnO_2$). With increasing $SnO_2$ in the mixed oxides, response towards ammonia increased at the optimum temperature 200°C as shown in Figure 7(a), whereas $WO_3$–(0.54)$SnO_2$ mixed oxide showed best sensing response for ethanol [Figure 7(b)]. However, pure $SnO_2$ nanoparticles sample was found to show maximum response in presence of acetone [Figure 7(c)].

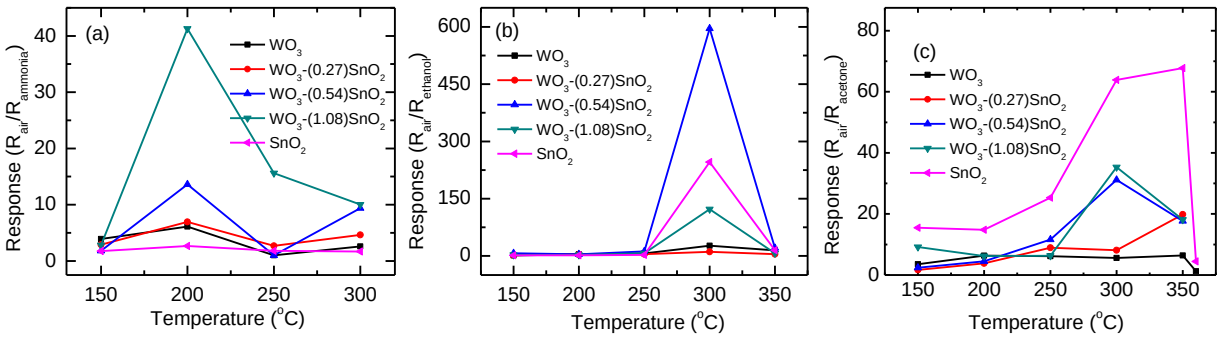


**Figure 7.** Response of different samples as a function of operating temperature towards (a) ammonia (1200 ppm), (b) ethanol (350 ppm), and (c) acetone (1000 ppm).

The sensing tests were further carried out for different concentrations of VOCs (ammonia – 400 to 2800 ppm, ethanol – 180 to 2800 ppm, and acetone – 1000 to 4000 ppm) using all the five samples [(i) $WO_3$, (ii) $WO_3$–(0.27)$SnO_2$, (iii) $WO_3$–(0.54)$SnO_2$, (iv) $WO_3$–(1.08)$SnO_2$, and (v) $SnO_2$]. The dynamic response-recovery curves with different VOC concentration are shown in Figure 8(a), 8(b), and 8(c) for ammonia, ethanol, and acetone, respectively. In particular, $WO_3$–(1.08)$SnO_2$ [iv of Figure 8(a)] shows 35 times (400 ppm) to 54 times (2800 ppm) response against ammonia, and $WO_3$–(0.54)$SnO_2$ [iii of Figure 8(b)] exhibits ~392 times (180 ppm) to 1476 times (at 2800 ppm) response towards ethanol. We have further performed the methanol sensing using $WO_3$–(0.54)$SnO_2$ (sample iii) at an optimum temperature of 300 °C (results not shown) which exhibits ~15 times response towards 1000 ppm methanol. Although the response was found to be much less than that of ethanol, mixed oxide can still be used for methanol sensing. This substantiates the important role of mixed oxides in the sensing performance of ammonia and ethanol. However, pure $SnO_2$ nanoparticles [v of Figure 8(b)] shows ~40 times (1000 ppm) to ~80 times (4000 ppm) response against acetone. The response of all the samples increased linearly with increase in concentration of ammonia and ethanol as shown in Figure 8(d) and 8(e), respectively. However, in case of acetone, response increases initially and then saturates at higher concentration as shown in Figure 7(f). This could be due to fact that at higher concentration the gas molecules do not find sufficient reaction sites. An anomaly of rapid decrease in response with time after reaching to maximum is observed for ammonia with $WO_3$–(1.08)$SnO_2$ [iv of Figure 8(a)]. This instability is believed to be due to structural transformation, materials poisoning, bulk diffusion, and/or generation of electron acceptor species such as $NO_x$ in the present case that abridges the sensing response.[39] Similar instability in

response as a function of time has been reported in recent literature.[40] Further study is needed to find the exact cause of such instability.

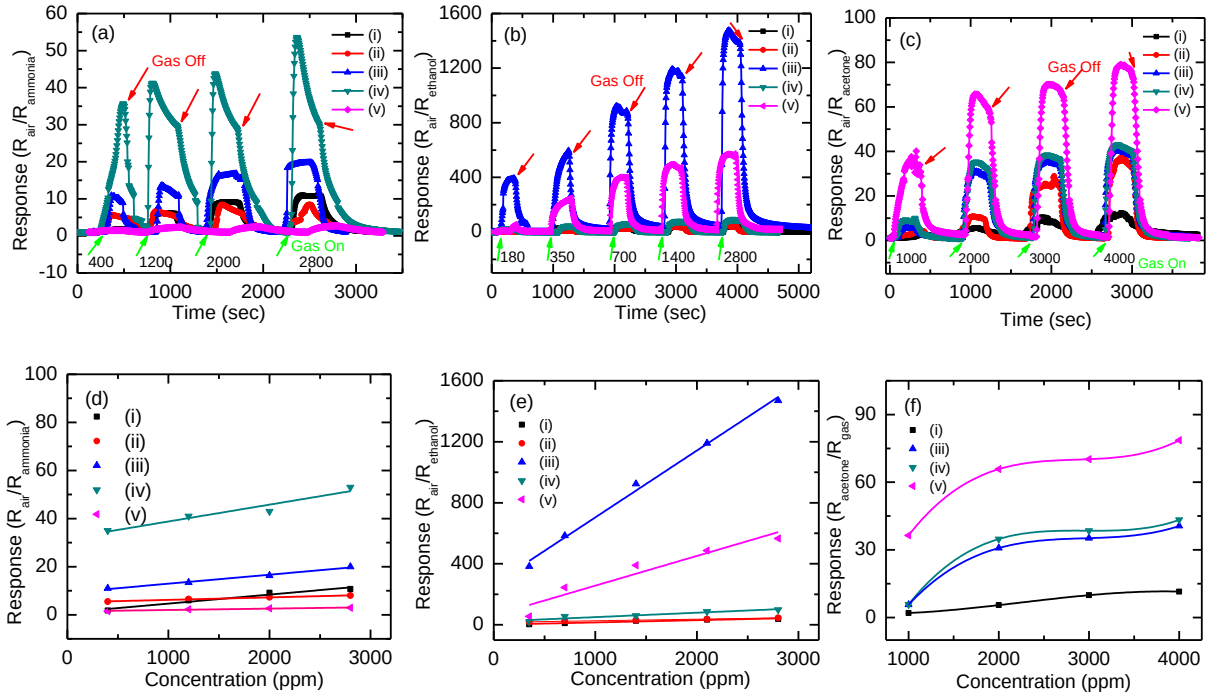


**Figure 8**. The dynamic response curves of five sensors with different gas concentrations for (a) ammonia at 200 °C, (b) ethanol at 300 °C, and (c) acetone at 300 °C as a function of time. The sensor materials are (i) $WO_3$, (ii) $WO_3$–(0.27)$SnO_2$, (iii) $WO_3$–(0.54)$SnO_2$, (iv) $WO_3$–(1.08) $SnO_2$, and (v) $SnO_2$. (d, e) Linear fitted response as a function of (d) ammonia and (e) ethanol concentration. (f) The third order polynomial fitted response as a function acetone concentration.

The lowest limit of detection (LOD) for all three VOCs was theoretically calculated from the experimental data obtained here. The details on LOD calculation is provided as supporting information. The LOD was calculated to be 520 ppb for ammonia, 131 ppb for ethanol, and 2.68 ppm for acetone. This suggests that these sensors can be used to detect trace levels of VOCs (except acetone which requires detection ability of ~1 ppm to be used) for biomedical applications and thus are suitable for breath analysis.[41] The performance of the best sensor

material for different VOCs is summarized in Table 1. The present result is further compared with recent literature on these VOCs and presented in Table 2. It is found that the sensing performance of present $WO_3$–$SnO_2$ mixed oxide is not only superior to several other oxide materials but also better than that of the noble metal doped/decorated oxides.[27,42,43,44,45,46,47,48,49,50]

**Table 1.** Summary on the Performance of Sensor Materials for Different VOCs

| VOCs | Sensor material with highest response | Response | | Optimum response temperature | Calculated LOD |
|---|---|---|---|---|---|
| | | with lowest VOC concentration | with highest VOC concentration | | |
| Ammonia | $WO_3$–(1.08) $SnO_2$ | 35 times (400 ppm) | 54 times (2800 ppm) | 200°C | 520 ppb |
| Ethanol | $WO_3$–(0.54) $SnO_2$ | 392 times (180 ppm) | 1476 times (2800 ppm) | 300°C | 131 ppb |
| Acetone | $SnO_2$ | 40 times (1000 ppm) | 80 times (4000 ppm) | 350°C | 2.68 ppm |

**Table 2.** Comparison of Best Sensing Performance of Different Materials towards Ammonia, Ethanol, and Acetone.

| VOCs | Sensing material | Concentration (Best Response) | Present Best Results | Ref. |
|---|---|---|---|---|
| Ammonia | Cr doped $WO_3$ | 50-500ppm(9-50 times) | 400 ppm (35 times) | 42 |
| Ammonia | Metal doped $SnO_2$ (Pt, Au, Cr, Pd, In, Cu) | 450 ppm (26 times) best with Pt | 400 ppm (35 times) | 43 |
| Ammonia | Metals doped $WO_3$ (Pd, Pt, Au) | 400-4000 ppm (4 – 44 times) | 400-2800 ppm (35-54 times) | 27 |
| Ethanol | $SnO_2$ | 1-1000 ppm (10-280 times) | 180-1500 ppm (400-1470 times) | 44 |
| Ethanol | $MoO_3$ | 10-500 ppm (10-50 times) | 180-1500 ppm (400-1470 times) | 45 |
| Ethanol | Gallia-$SnO_2$ | 300 ppm (120 times) | 350 ppm (600 times) | 46 |
| Ethanol | $WO_3$ | 10-500 ppm (1.5-2.4 times) | 350 ppm (600 times) | 47 |
| Ethanol and ammonia | $SnO_2$/ZnO | Ethanol 25-500ppm (3-17 times) Ammonia 100ppm(2 times) | Ethanol 350 ppm (600 times) Ammonia 100 ppm (35 times) | 48 |
| Acetone | $SnO_2$-Pt | 800 ppm(3.3 times) | 1000 ppm (37 times) | 49 |
| Acetone | $WO_3$ | 1000 ppm(20 times) | 1000 ppm (37 times) | 50 |

The sensing results revealed an apparent temperature-dependent selectivity towards the VOCs as shown in Figure 7 *i.e.* 200°C for ammonia, 300°C for ethanol, and 350°C for acetone. To further explore their selectivity, the best sensing samples were exposed to toluene, hexane, and chloroform because all these vapors have biological or environmental consequences. Figure 9(a), 9(b), and 9(c) show the comparative response bar plots of different VOCs with 1200 ppm at 200°C [using $WO_3$–(1.08)$SnO_2$], with 350 ppm at 300°C [using $WO_3$–(0.54)$SnO_2$], and with

2000 ppm at 350°C [using $SnO_2$], respectively. A stand out temperature-dependent selective response can be clearly noticed for the respective analytes.

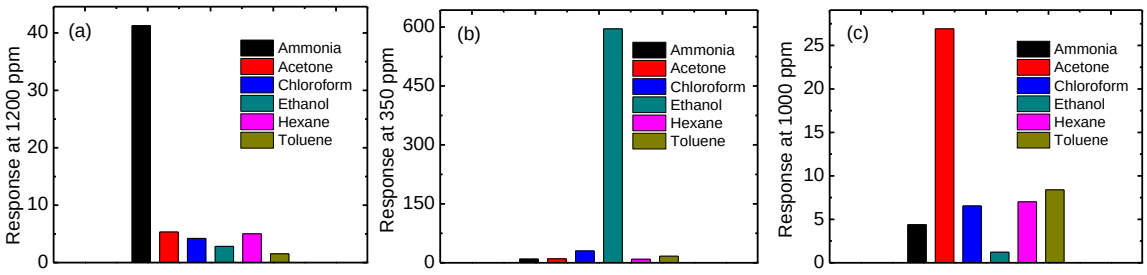


**Figure 9.** Comparative response bar plots of different VOCs (a) with 1200 ppm at 200 ºC using $WO_3$–(1.08)$SnO_2$, (b) with 350 ppm at 300ºC using $WO_3$–(0.54)$SnO_2$ sample, and (c) with 2000 ppm at 350 ºC using $SnO_2$ sample.

**Sensing mechanism**

The optimum responses towards three analytes were observed in three different samples, *e.g.* the best response against ammonia, ethanol, and acetone was shown by $WO_3$–(1.08)$SnO_2$, $WO_3$–(0.54)$SnO_2$, and $SnO_2$, respectively. For almost all the samples, optimum response occurred at three different temperatures, *e.g.* at 200°C for ammonia, at 300°C for ethanol, and at 350°C for acetone.

***Effect of Sensing Material.*** The sensing mechanism of the heterogeneous metal oxide structure is explained through schematics shown in Figure 10.

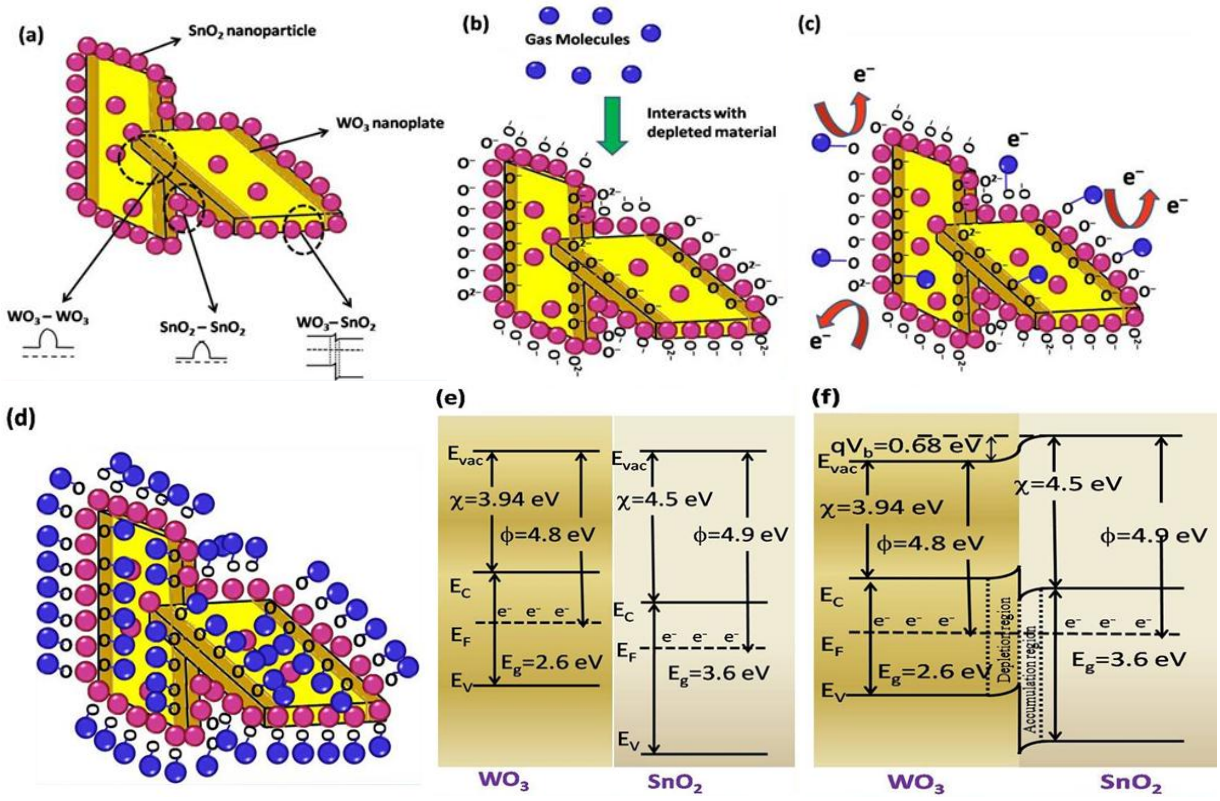


**Figure 10.** Schematic representation of (a) $WO_3$–$SnO_2$ mixed oxides with available barrier potentials, (b) different species of oxygen adsorbed on the surface of the heterostructured metal oxide upon exposed to dry air, (c) reaction and attachment of gas molecules with the adsorbed oxygen, (d) complete covering of active sites with the gas molecules, (e) energy band structure of $WO_3$ and $SnO_2$, and (f) energy band structure of $WO_3$-$SnO_2$ mixed metal oxide.

The basic mechanism of sensing by metal oxide has been discussed in details in the literature.[17] Briefly, when air comes in contact with metal oxide surface, the oxygen molecules in air get adsorbed and form different oxygen species ($O^-$, $O^{2-}$, $O_2^-$, and $O_2^{2-}$) by trapping the free surface electrons from the conduction band of n-type sensing layer ($WO_3$ and $SnO_2$) as shown in Figure 10(b). This leads to electron depletion on the metal oxide surface, which contributes toward large base line resistance of the sensing material. These adsorbed oxygen sites act as active sites for the targeted gas molecules to get attached. Upon introducing target reducing gases such as ammonia, ethanol, and acetone, they are oxidized by reactive oxygen species,

resulting release of electrons to the sensing material (metal oxide) and thereby its resistance decreases. To explain the effect of material on the sensor performance, the following points are needed to be considered.

First, in a $WO_3$–$SnO_2$ mixed oxide heterostructure, the electron transport mechanism is different from that of individual metal oxides ($WO_3$ and $SnO_2$) because of the presence of multiple junctions. In $WO_3$–$SnO_2$ mixed oxide, three different potential barriers exist and those are between $WO_3$ and $WO_3$, $WO_3$ and $SnO_2$, and $SnO_2$ and $SnO_2$. The schematic band diagram of $WO_3$–$SnO_2$ heterojunction is shown in Figure 10 (e, f). As the position of the Fermi level in $WO_3$ is higher than that of $SnO_2$, electron transfer takes place from $WO_3$ to $SnO_2$ by bend bending and a potential barrier is established at the heterojunction as shown in the Figure 10(f). These two kinds of potential barriers (two potential barriers at homojunctions and one potential barrier at heterojunction) hinder the electron transport through the nanostructures. Thus they provide extra electrons for more oxygen species to adsorb on the surface of the sensing layer, which significantly increases the sensor response.

Second, ethanol decomposition [equation (2) and (3)] is related to the acid-base property of the mixed metal oxides.[51]

$$C_2H_5OH \rightarrow C_2H_4 + H_2O \text{ (acidic oxide)} \quad (2)$$

$$C_2H_5OH \rightarrow CH_3CHO + H_2 \text{ (basic oxide)} \quad (3)$$

$WO_3$ is acidic in nature, whereas $SnO_2$ has both acidic and basic properties.[51,52] In case of $WO_3$, only dehydration to intermediate $C_2H_4$ is expected, whereas both dehydration and dehydrogenation would occur in case of mixed oxide. The intermediate states ($CH_3CHO$ and $C_2H_4$) can react with oxygen ions to produce $CO_2$ and $H_2O$ [equation (4) and (5)]. These

reactions also release electrons which decrease the sensing layer resistance. Thus, $WO_3$–$SnO_2$ mixed oxide gives larger ethanol response compared to a single metal oxide.

$$CH_3CHO + 5O^- \rightarrow 2CO_2 + 2H_2O + 5e^- \quad (4)$$

$$C_2H_4 + 6O^- \rightarrow 2CO_2 + 2H_2O + 6e^- \quad (5)$$

Third, there has been a recent report that the heterostructure's sensing performance also depend on the ability of the test molecules to reach at the heterojunction.[53] As the size of ammonia molecule is smallest (kinetic diameter 0.26 nm)[54] among the three chemical analytes tested in this work, ammonia has the maximum probability to reach not only at depleted homojunctions ($SnO_2$/$SnO_2$ and $WO_3$/$WO_3$), but also at $SnO_2$/$WO_3$ depleted heterojunctions. The kinetic diameter of ethanol and acetone molecule is 0.45 nm and 0.469 nm, respectively.[53] In the present case, the highest density of $SnO_2$ particles on $WO_3$ nanoplates is found in sample iv [$WO_3$–(1.08)$SnO_2$], which shows highest sensitivity towards ammonia. The high selectivity of ammonia towards sample iv [$WO_3$–(1.08)$SnO_2$] is thus attributed to highest $SnO_2$ density (thereby maximum heterojunction area) and the smaller kinetic diameter of ammonia allowing it to reach to the junction at the interface of $WO_3$ and $SnO_2$. However, as the molecular size of ethanol molecule is larger than that of ammonia, ethanol molecules have less probability to reach at all the heterojunctions where $SnO_2$ nanoparticles are agglomerated on $WO_3$ nanoplates as evident from FESEM image [Figure 1(f)]. Hence the sensitivity towards ethanol is lower for sample iv [$WO_3$–(1.08)$SnO_2$] with dense $SnO_2$ nanoparticles. But in case sample iii [$WO_3$–(0.54)$SnO_2$], all the ethanol molecules can access both the homo and heterojunctions due to evenly dispersed $SnO_2$ nanoparticles on $WO_3$ nanoplates. Hence ethanol sensitivity is found to be highest for sample iii. This argument can similarly be applicable for the acetone because of its

largest kinetic diameter among the VOCs we have chosen. Thus sensing layer with heterojunction is less effective for acetone.

Fourth, the particle size is also known to play a critical role in gas sensing behavior.[55] A good approximation of the optimal particle size for gas sensing applications can be obtained from the Debye length. It is well known that a particle with nearly twice that of Debye length depletes completely when interact with oxygen molecules and thus the whole particle can take part in gas sensing. In case of $SnO_2$, the Debye length is around 3 nm at 250°C and it increases ($\propto\sqrt{T}$) with temperature.[56] This explains why $SnO_2$ sample (particle size 5–10 nm) exhibits highest sensitivity towards acetone compared to other samples. Thus the heterojunction depletion layer did not play a critical role in case of acetone rather the large surface to volume ratio of $SnO_2$ nanoparticles (concentration of increased adsorbed oxygen species) was the major factor.

Another factor that plays an important role in sensing behaviour is the porosity of hierarchical material.[57,58,59] The Knudsen diffusion and molecular gas diffusion processes are described for the smaller (2–100 nm) and larger (above 100 nm) pore diameter of sensing material.[60] Thus we have further measured the effective BET surface area and porosity of as-synthesized materials. Figure 11 displays the nitrogen adsorption-desorption isotherms of (a) $WO_3$ nanoplates, (b) $SnO_2$ nanoparticles, (c) $WO_3$–(0.54)$SnO_2$, and (d) $WO_3$–(1.08)$SnO_2$ samples. The effective surface area is measured to be the largest (19.5 $m^2/g$) for $SnO_2$ nanoparticles and the lowest (11.38 $m^2/g$) for $WO_3$ nanoplates as expected. The effective surface area of $WO_3$–(0.54)$SnO_2$ and $WO_3$–(1.08)$SnO_2$ was measured to be 13.87 and 17.9 $m^2/g$, respectively. The average pore size was estimated to be in the range of 25 to 35 nm suggesting mesoporous samples. Although, the effective BET surface area of as-synthesized samples is highly correlated to the surface morphology, the sensing behaviour of samples is found to be not

directly depended on the surface area. This confirms the important role of heterojunction in the sensing material along with sensing gases and temperature.

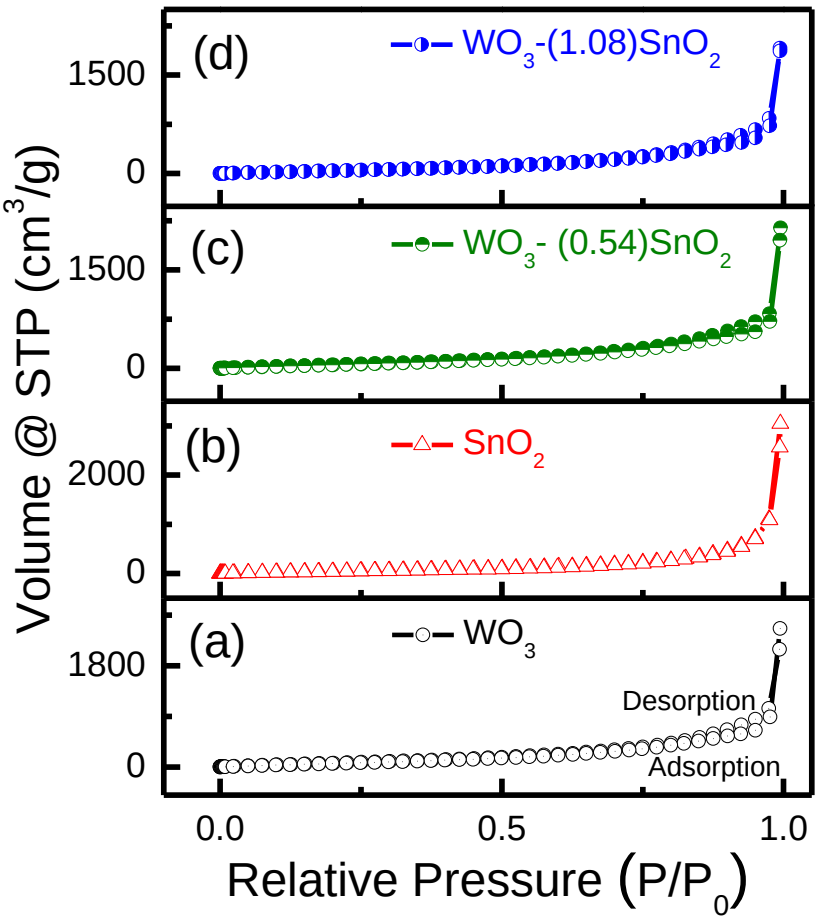


**Figure 11.** Nitrogen adsorption-desorption isotherm of the (a) $WO_3$ nanoplates, (b) $SnO_2$ nanoparticles, (c) $WO_3$–(0.54)$SnO_2$, and (d) $WO_3$–(1.08)$SnO_2$.

***Effect of Temperature.*** The present VOC sensing behavior clearly ascertains the temperature-dependent gas selectivity as outlined before. It is known that at lower temperature (<200ºC), $O_{2(ads)}^{-}$ and $O_{2(ads)}^{2-}$ are predominant whereas at higher temperature, atomic reactants $O_{(ads)}^{-}$ and $O_{(ads)}^{2-}$ are found in abundance.[61]

First, in case of ammonia, following reactions [equation (6) and (7)] are feasible.[61]

At 200ºC, $4NH_3 + 3O_{2(ads)}^{-}$ (or $3O_{2(ads)}^{2-}$) $\rightarrow 2N_2 + 6H_2O + 3e^{-}$ (or $6e^{-}$) (6)

At 300ºC, $2NH_3 + 3O_{(ads)}^{-}$ (or $3O_{(ads)}^{2-}$) $\rightarrow N_2 + 3H_2O + 3e^{-}$ (or $6e^{-}$) (7)

The above chemical reactions show release of same number of electrons at lower and higher temperature. But along with the aforementioned reactions, the oxidation reactions that occur primarily depend on the operating temperature and nature of metal oxides. This will lead to formation of $NO_x$ as shown in the reactions (8) and (9) below.[42,62]

$NH_3 + 4O^{-} \rightarrow N_2O + 3H_2O + 4e^{-}$ (8)

$NH_3 + 5O^{-} \rightarrow 2NO + 3H_2O + 5e^{-}$ (9)

Thus, at higher temperature, $NH_3$ being the donor molecule results in decrease in resistance of the metal oxides, alongside $NO_x$ being acceptor molecules withdraw electrons, thereby resulting in increase in resistance of the $WO_3$–$SnO_2$ sensors. Hence, the effective response of the nanoparticles towards ammonia decreases at higher temperatures.

The following chemical reactions [equation (10) and (11)] could occur on the surface of sensing material for the case of ethanol.[63]

At 200ºC, $CH_3CH_2OH + 3O_{2(ads)}^{-}$ (or $3O_{2(ads)}^{2-}$) $\rightarrow 2CO_2 + 3H_2O + 3e^{-}$ (or $6e^{-}$) (10)

At 300ºC, $CH_3CH_2OH + 6O_{(ads)}^{-}$ ($6O_{(ads)}^{2-}$) $\rightarrow 2\ CO_2 + 3H_2O + 6e^{-}$ (or $12e^{-}$) (11)

Our experimental results showed maximum ethanol response at 300ºC for all the samples suggesting higher interaction on the surface. However, at a higher temperature (350ºC), the

ethanol-metal oxide interaction is expected to be weakened resulting poor response, as shown in the reaction [equation (12)] below.[64]

At 350°C, $CH_3CH_2OH + O_{(ads)}^{2-} \rightarrow CH_3CHO + H_2O + 2e^-$ (12)

On the other hand, acetone releases only single electron when reacts with oxygen ions below 300°C [equation (13)]. So the change in sensing layer resistance is less. However, above 300°C the number of electrons released is much higher as shown in the reaction below [equation (14)]. This is believed to be due to insufficient active sites at lower temperature (<300°C) for all the molecules to be oxidized, whereas at higher temperature (350ºC), the reaction products get desorbed at a faster rate and hence the new gas species find enough active sites for attachment.[64]

At <300°C, $CH_3COCH_3 + O_{(ads)}^- \rightarrow CH_3COC^+H_2 + OH^- + e^-$ (13)

At >300°C, $CH_3COCH_3 + 8O_{(ads)}^-$ (or $8O_{(ads)}^{2-}$) $\rightarrow 3CO_2 + 3H_2O + 8e^-$ ($16e^-$) (14)

This is attributed to the maximum response obtained at 350ºC in the case of acetone.

## Conclusions

Here, we demonstrate the synergy of two active oxide materials *i.e.* $WO_3$ nanoplates and $SnO_2$ nanoparticles for the temperature-dependent sensing behavior of three important biomarkers (ammonia, ethanol, and acetone). The $SnO_2$ nanoparticle size and density on $WO_3$ nanoplates was controlled by varying the $SnCl_2 \cdot 2H_2O$ precursor using a facile *in situ* hydrothermal synthesis technique. This leads to optimum ratio of $SnO_2$ nanoparticles on $WO_3$ nanoplates, which played a crucial role in the sensing selectivity of VOCs. In particular, smaller kinetic diameter of the ammonia molecules easily approached the interface of $WO_3$–$SnO_2$ junction in case of high density $SnO_2$ nanoparticles covered $WO_3$ nanoplates sample showing maximum sensitivity. On the other hand, best performance was obtained for ethanol with sparsely coated $SnO_2$

nanoparticles on $WO_3$ nanoplates due to the bigger kinetic diameter of ethanol molecules. The higher sensing performance in the present work than the previous reports is attributed to formation of heterojunction at the interface of two oxides. The as-fabricated chemoresistive sensor using the noble-metal free oxide materials has strong potential for biomedical and environmental applications both in terms of cost effectiveness and performance.

**Acknowledgements**

D. Pradhan and P. K. Guha acknowledge SRIC, IIT Kharagpur (ISIRD) for partial support of this work. S. Santra acknowledges Department of Science and Technology (DST), India for the partial support of the work (project no SR/S2/RJN-104/2011). Authors also acknowledge the DST-FIST funded facility at the Department of Physics for XPS measurement.

**References and Notes**

1 J. W. Gardner, P. K.Guha, F. Udrea, J. A. Covington, CMOS Interfacing for Integrated Gas Sensors: A Review, *IEEE Sens. J.* 2010, **10**, 1833–1848.

2 W. Q. Cao, Y. X. Duan, Current Status of Methods and Techniques of Breath Analysis. *Crit Rev. Anal. Chem.* 2007, **37**, 3–13.

3 R. Mukhopadhyay, Don't Waste your Breath. *Anal. Chem.* 2004, **76**, 273A–276A.

4 J. M.Sanchez, R. D. Sacks, GC Analysis of Human Breath with a Series-Coupled Column Ensemble and A Multibed Sorption Trap. *Anal. Chem.* 2003, **75**, 2231–2236.

5 M. Li, J. Ding, H. Gu, Y. Zhang, S. Pan, N. Xu, H. Chen, H. Li, Facilitated Diffusion of Acetonitrile Revealed by Quantitative Breath Analysis Using Extractive Electrospray Ionization Mass Spectrometry. *Scientific Reports* 2013, **3**, Article number 1205.

6 M. Righettoni, A.Tricoli, Toward Portable Breath Acetone Analysis for Diabetes Detection.

*J. Breath Res.* 2011, **5**, 037109.

[7] V. E. Bochenkov, G. B. Sergeev, Sensitivity, selectivity, and stability of gas-sensitive metal-oxide nanostructures. Chapter 2, Page 31–52, Metal Oxide Nanostructures and Their Applications (Edited by A. Umar and Y. -B. Hahn) American Scientific Publishers 2010.

[8] A. Tricoli, M. Righettoni, A. Teleki, Semiconductor Gas Sensors: Dry Synthesis and Application. *Angew. Chem. Int. Ed.*2010, **49**, 7632 – 7659.

[9] S. Elouali, L. G. Bloor, R. Binions, I. P. Parkin, C. J. Carmalt, J. A. Darr, Gas Sensing with Nano-Indium Oxides ($In_2O_3$) Prepared via Continuous Hydrothermal Flow Synthesis. *Langmuir* 2012, **28**, 1879−1885.

[10] M. Kimura, R. Sakai, S. Sato, T. Fukawa, T. Ikehara, R. Maeda, T. Mihara, Sensing of Vaporous Organic Compounds by $TiO_2$ Porous Films Covered with Polythiophene Layers. *Adv. Funct. Mater*. 2012, **22**, 469–476.

[11] S. Santra, P. K. Guha, S. Z. Ali, P. Hiralal, H. E. Unalan, J. A. Covington, G. A. J. Amaratunga, W. I. Milne, J. W. Gardner, F. Udrea, ZnO nanowires grown on SOI CMOS substrate for ethanol sensing. *Sens. Actuators, B* 2010, **146**, 559–565.

[12] D. P. Volanti, A. A. Felix, M. O. Orlandi, G. Whitfield, D.-J. Yang, E. Longo, H. L. Tuller, J. A. Varela, The Role of Hierarchical Morphologies in the Superior Gas Sensing Performance of CuO-Based Chemiresistors. *Adv. Funct. Mater*. 2013, **23**, 1759–1766.

[13] Y. Shen, T. Yamazaki, Z. Liu, D. Meng, T. Kikuta, N. Nakatani, Influence of Effective Surface Area on Gas Sensing Properties of $WO_3$ Sputtered Thin Films. *Thin Solid Films* 2009, **517**, 2069–2072.

[14] D. Chen, X. Hou, T. Li, L. Yin, B. Fan, H. Wang, X. Li, H. Xu, H. Lu, R. Zhang, J. Sun, Effects of Morphologies on Acetone-sensing Properties of Tungsten Trioxide Nanocrystals. *Sens. Actuators, B* 2011, **153**, 373–381.

[15] J. Shi, G. Hu, Y. Sun, M. Geng, J. Wu, Y. Liu, M. Ge, J. Tao, M. Cao, N. Dai, $WO_3$ Nanocrystals: Synthesis and Application in Highly Sensitive Detection of Acetone. *Sens. Actuators, B* 2011, **156**, 820–824.

[16] N. D. Hoa, S. A. El-Safty, Gas Nanosensor Design Packages Based on Tungsten Oxide: Mesocages, Hollow Spheres, and Nanowires. *Nanotechnology* 2011, **22**, 485503 (10pp).

[17] F. Fang, J. Kennedy, J. Futter, T. Hopf, A. Markwitz, E. Manikandan, G. Henshaw, Size-controlled Synthesis and Gas Sensing Application of Tungsten Oxide Nanostructures Produced by Arc Discharge. *Nanotechnology* 2011, **22**, 335702 (7pp).

[18] S. Piperno, M. Passacantando, S. Santucci, L. Lozzi, S. L. Rosa, $WO_3$ Nanofibres for Gas Sensing Applications. *J. Appl. Phys*. 2007, **101**, 124504-124504.

[19] A. Ponzoni, V. Russo, A. Bailini, C.S. Casari, M. Ferroni, A. Li Bassi, A. Migliori, V. Morandi, L. Ortolani, G. Sberveglieri, C.E. Bottani, Structural and Gas-sensing Characterization of Tungsten Oxide Nanorods and Nanoparticles. *Sens. Actuators, B* 2011, **153**, 340–346.

[20] R. K. Joshi, F. E. Kruis, O. Dmitrieva, Gas Sensing Behavior of $SnO_{1.8}$:Ag Films Composed of Size-selected Nanoparticles. *J. Nanopart. Res.* 2006, **8**, 797–808.

[21] H. Xia, Y. Wang, F. Kong, S. Wang, B. Zhu, X. Guo, J. Zhang, Y. Wang, S. Wu, Au-doped $WO_3$-based Sensor for $NO_2$ Detection at Low Operating Temperature. *Sens. Actuators, B* 2008, **134**, 133–139.

[22] A. Esfandiara, A. Irajizada, O. Akhavana, S. Ghasemic, M. R. Gholamic, Pd–$WO_3$/Reduced Graphene Oxide Hierarchical Nanostructures as Efficient Hydrogen Gas Sensors. *Int. J. Hydrogen Energy* 2014, **39**, 8169–8179.

[23] V. S. Solntsev, T. I. Gorbanyuk, V. G. Litovchenko, A. A. Evtukh, MIS Gas Sensors Based on Porous Silicon with Pd and $WO_3$/Pd Electrodes. *Thin Solid Films* 2009, **517**, 6202–6205.

[24] Y. Zhao, X. Lai, P. Deng, Y. Nie, Y. Zhang, L. Xing, X. Xue, Pt/ZnO Nanoarray Nanogenerator as Self-powered Active Gas Sensor with Linear Ethanol Sensing at Room Temperature. *Nanotechnology* 2014, **25**, 115502 (6pp).

[25] J. Fu, C. Zhao, J. Zhang, Y. Peng, E. Xie, Enhanced Gas Sensing Performance of ElectrospunPt-Functionalized NiO Nanotubes with Chemical and Electronic Sensitization. *ACS Appl. Mater. Interfaces* 2013, **5**, 7410–7416.

[26] S. J. Ippolito, S. Kandasamy, K. Kalantar-zadeh, W. Wlodarski, Hydrogen Sensing Characteristics of $WO_3$ Thin Film Conductometric Sensors Activated by Pt and Au catalysts. *Sens. Actuators, B* 2005, **108**, 154–158.

[27] V. Srivastava, K. Jain, Highly Sensitive $NH_3$ Sensor Using Pt Catalyzed Silica Coating over $WO_3$ Thick Films. *Sens. Actuators, B* 2008, **133**, 46–52.

[28] I. Jimenez, M. A. Centeno, R. Scotti, F. Morazzoni, J. Arbiol, A. Cornet, J. R. Morante, $NH_3$ Interaction with Chromium-doped $WO_3$ Nanocrystalline Powders for Gas Sensing Applications. *J. Mater. Chem.* 2004, **14**, 2412–2420.

[29] M. Righettoni, A. Tricoli, S.E. Pratsinis, Si:$WO_3$ Sensors for Highly Selective Detection of Acetone for Easy Diagnosis of Diabetes by Breath Analysis. *Anal. Chem*. 2010, **82**, 3581–3587.

[30] S. B. Upadhyay, R. K. Mishra, P.P. Sahay, Structural and Alcohol Response Characteristics of Sn-doped $WO_3$ Nanosheets. *Sens. Actuators, B* 2014, **193**, 19– 27.

[31] H. -R. Kim , A. Haensch , I. -D. Kim , N. Barsan , U. Weimar, J.-H. Lee, The Role of NiO Doping in Reducing the Impact of Humidity on the Performance of $SnO_2$-Based Gas Sensors: Synthesis Strategies, and Phenomenological and Spectroscopic Studies. *Adv. Funct. Mater.* 2011, **21**, 4456–4463.

[32] L. Xu, H. Song, B. Dong, Y. Wang, J. Chen, X. Bai, Preparation and Bifunctional Gas Sensing Properties of Porous $In_2O_3$−$CeO_2$ Binary Oxide Nanotubes. *Inorg. Chem*. 2010, **49**, 10590–10597.

[33] T. Kida, A. Nishiyama, Z. Hua, K. Suematsu, M. Yuasa, K. Shimanoe, $WO_3$ Nanolamella Gas Sensor: Porosity Control Using $SnO_2$ Nanoparticles for Enhanced $NO_2$ Sensing. *Langmuir* 2014, **30**, 2571−2579.

[34] F. Y. Xie, L. Gong, X. Liu, Y. T. Tao, W. H. Zhang, S. H. Chen, H. Meng, J. Chen. XPS Studies on Surface Reduction of Tungsten Oxide Nanowire Film by Ar+ Bombardment. *J. Electron Spectrosc. Relat. Phenom.* 2012, **185**, 112–118.

[35] K. Senthil, K.Yong. Growth and Characterization of Stoichiometric Tungsten Oxide Nanorods by Thermal Evaporation and Subsequent Annealing. *Nanotechnology* 2007, **18**, 395604 (7pp).

[36] Y. Baek, K. Yong, Controlled Growth and Characterization of Tungsten Oxide Nanowires Using Thermal Evaporation of $WO_3$ Powder. *J. Phys. Chem. C* 2007, **111**, 1213–1218.

[37] S. Bazargan, N. F. Heinig, D. Pradhan, K. T. Leung, Controlled Growth of Monodisperse Nanocrystallites in Tin(IV) Oxide Nanofilms. *Crys. Growth Des.* 2011, **11**, 247–255.

[38] S. Yan, Q. Wu, Micropored Sn-$SnO_2$/carbon Heterostructure Nanofibers and Their Highly Sensitive and Selective $C_2H_5OH$ Gas Sensing Performance. *Sens. Actuators, B* 2014, **205**, 329–337.

[39] G. Korotcenkova, B. K. Cho, Instability of metal oxide-based conductometric gas sensors and approaches to stability improvement (short survey). *Sens. Actuators, B* 2011, **156**, 527– 538.

[40] L. Wang, P. Gao, D. Bao, Y. Wang, Y. Chen, C. Chang, G. Li, P. Yang, Synthesis of Crystalline/Amorphous Core/Shell $MoO_3$ Composites through a Controlled Dehydration Route and Their Enhanced Ethanol Sensing Properties. Cryst. Growth Des. 2014, **14**, 569−575

[41] C. Deng, J. Zhang, X. Yu, W. Zhang, X. Zhang, Determination of Acetone in Human Breath by Gas Chromatography–mass Spectrometry and Solid-phase Microextraction with On-fiber Derivatization. *J. Chromatogr. B* 2004, **810**, 269–275.

[42] M. Epifani, T. Andreu, C. R. Magana, R. Diaz, J. Arbiol, P. Siciliano, J. R. Morante, From Doping to Phase Transformation: Ammonia Sensing Performances of Chloroalkoxide-derived $WO_3$ Powders Modified with Chromium. *Sens. Actuators, B* 2010, **148**, 200–206.

[43] Md. Shahabuddin, A. Sharma, J. Kumar, M. Tomar, A. Umar, V. Gupta, Metal Clusters Activated $SnO_2$ Thin Film for Low Level Detection of $NH_3$ Gas. *Sens. Actuators, B* 2014, **194**, 410–418.

[44] M. M. Natile, A. Ponzoni, I. Concina, A. Glesenti, Chemical Tuning Versus Microstructure Features in Solid-State Gas Sensors: $LaFe_{1-x}Ga_xO_3$, a Case Study. *Chem. Mater.* 2014, **26**, 1505–1513.

[45] L. Wang, P. Gao, D. Bao, Y. Wang, Y. Chen, C. Chang, G. Li, P. Yang, Synthesis of Crystalline/amorphous Core/shell $MoO_3$ Composites Through Controlled Dehydration Route and Their Enhanced Ethanol Sensing Properties. *Cryst.Growth Des.* 2014, **14**, 569–575.

[46] M. Bagheri, A. A. Khodadadi, A. R. Mahajoub, Y. Mortazavi, Highly Sensitive Gallia-$SnO_2$ Nanocomposite Sensors to CO and Ethanol in Presence of Methane. *Sens. Actuators, B* 2013, **188**, 45–52.

[47] J. Ma, J. Zhang, S.Wang, T. Wang, J. Lian, X. Duan, W. Zheng. Topochemical Preparation of $WO_3$ Nanoplates through Precursor $H_2WO_4$ and Their Gas-Sensing Performances. *J. Phys. Chem. C* 2011, **115**, 18157–18163.

[48] N. D. Khoang, D. D. Trung, N. V. Duy, N. D. Hoa, N. V. Hieu, Design of $SnO_2$/ZnO Hierarchical Nanostructures for Enhanced Ethanol Gas-sensing Performance. *Sens. Actuators, B* 2012, **174**, 594–601.

[49] X. Li, J. H. Cho, P. Kurup, Z.Gu, Novel Sensor Array Based on Doped Tin Oxide Nanowires for Organic Vapor Detection. *Sens. Actuators, B* 2012, **162**, 251–258.

[50] D. Chen, X. Hou, T. Li, L.Yin, B. Fan, H. Wang, X. Li, H. Xu, H. Lu, R. Zhang, Effects of Morphologies on Acetone-sensing Properties of Tungsten Trioxide Nanocrystals. *Sens. Actuators, B* 2011, **153**, 373–381.

[51] H. -W. Cheong, M. -J. Lee. Sensing Characteristics and Surface Reaction Mechanism of Alcohol Sensors based on Doped $SnO_2$. *J. Ceram. Process. Res.* 2006, **7**, 183–191.

[52] T. Kim, A. Burrows, C. J. Kiely, I. E. Wachs, Molecular/electronic Structure–surface Acidity Relationships of Model-supported Tungsten Oxide Catalysts. *J. Catal.* 2007, **246**, 370–381.

[53] T. Rakshit, S. Santra, I. Manna, S. K. Ray, Enhanced Sensitivity and Selectivity of Brush-like $SnO_2$ Nanowire/ZnO Nanorod Heterostructure based Sensors for Volatile Organic Compounds. *RSC Adv.* 2014, **4**, 36749–36756.

[54] M. Kanezashi, A. Yamamoto, T. Yoshioka, T. Tsuru, Characteristics of Ammonia Permeation through Porous Silica Membranes. *AIChE J.* 2010, **56**, 1204–1212

[55] X. Du, S. M. George, Thickness Dependence of Sensor Response for CO Gas Sensing by Tin Oxide Films Grown using Atomic Layer Deposition. *Sens. Actuators, B* 2008, **135**, 152–160.

[56] H. Ogawa, M. Nishikawa, A. Abe, Hall Measurement Studies and An Electrical Conduction Model of Tin Oxide Ultrafine Particle Films. *J. Appl. Phys.* 1982, **53**, 4448–4455.

[57] F. Meng, S. Ge, Y. Jia, B. Sun, Y. Sun, C. Wang, H. Wu, Z. Jin, M. Li, Interlaced nanoflake-assembled flower-like hierarchical ZnO microspheres prepared by bisolvents and their sensing properties to ethanol. *J. Alloys Compd.* 2015, **632**, 645–650.

[58] F. Meng, N. Hou, S. Ge, B. Sun, Z. Jin, W. Shen, L. Kong, Z. Guo, Y. Sun, H. Wu, C. Wang, M. Li, Flower-like hierarchical structures consisting of porous single-crystalline ZnO nanosheets and their gas sensing properties to volatile organic compounds (VOCs). *J. Alloys Compd.* 2015, **626**, 124–130.

[59] H. Li, F. Meng, J. Liu, Y. Sun, Z. Jin, L. Kong, Y. Hu, J. Liu, Synthesis and gas sensing properties of hierarchical meso-macroporous $SnO_2$ for detection of indoor air pollutants. *Sens. Actuators, B* 2012, **166–167**, 519– 525.

[60] G. Sakai, N. Matsunaga, K. Shimanoe, N. Yamazoe, Theory of gas-diffusion controlled sensitivity for thin film semiconductor gas sensor, *Sens. Actuators B* 2001, **80**, 125–131

[61] K. Wetchakun, T. Samerjai, N. Tamaekong, C. Liewhiran, C. Siriwong, V. Kruefu, A. Wisitsoraat, A. Tuantranont, S. Phanichphant, Semiconducting Metal Oxides as Sensors for Environmentally Hazardous Gases. *Sens. Actuators, B* 2011, **160**, 580–591.

[62] V. Modafferi, G. Panzera, A. Donato, P. L. Antonucci, C. Cannilla, N. Donato, D. Spadaro, G. Neri, Highly Sensitive Ammonia Resistive Sensor based on Electrospun $V_2O_5$ Fibers. *Sens. Actuators, B* 2012, **163**, 61–68.

[63] M. Z.Ahmad, A. Z. Sadek, K. Latham, J. Kita, R. Moos, W. Wlodarski, Chemically Synthesized One-dimensional Zinc Oxide Nanorods for Ethanol Sensing. *Sens. Actuators, B* 2013, **187**, 295–300.

[64] R. S. Khadayate, J. V. Sali, P. P. Patil, Acetone Vapor Sensing Properties of Screen Printed $WO_3$ Thick films. *Talanta* 2007, **72**, 1077–1081.

# Table of Content Graphic

## Hierarchical Nanostructured $WO_3$–$SnO_2$ for Selective Sensing of Volatile Organic Compounds

Arpan Kumar Nayak, Ruma Ghosh, Sumita Santra, Prasanta Kumar Guha, Debabrata Pradhan*

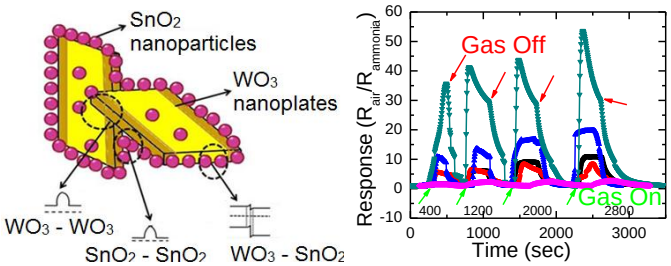


$WO_3$–$SnO_2$ mixed oxide is demonstrated as a suitable sensing material for volatile organic compounds with much improved sensitivity and selectivity.